Wang, Y. & Liatsis, P. (2012). Automatic Segmentation of Coronary Arteries in CT Imaging in the Presence of Kissing Vessel Artifacts. IEEE Transactions on Information Technology in Biomedicine, 16(4), pp. 782-788. doi: 10.1109/TITB.2012.2192286

Automatic Segmentation of Coronary Arteries in CT Imaging in the Presence of Kissing Vessel Artifacts

Yin Wang and Panos Liatsis, Member, IEEE

Abstract—In this paper, we present a novel two-step algorithm for segmentation of coronary arteries in CT images based on the framework of active contours. In the proposed method, both global and local intensity information are utilised in the energy calculation. The global term is defined as a normalised cumulative distribution function (CDF), which contributes to the overall active contour energy in an adaptive fashion based on image histograms, to deform the active contour to out of stationary points. Possible outliers, such as kissing vessel artifacts, are removed in post-processing stage by a slice-by-slice correction scheme based on multiple regions competition, where both arteries and kissing vascular structures are identified and tracked through the slices. We demonstrate the efficiency and the accuracy of the proposed technique on both synthetic and real datasets. The results on clinical datasets show that our method is able to extract the major branches of arteries with an average distance of 0.73 voxels to the manually delineated ground truth data. In the presence of kissing vessel artifacts, the outer surface of the entire coronary tree, extracted by the proposed algorithm is smooth and contains fewer erroneous regions, originating in the kissing vessel artifacts, as compared to initial segmentation.

Index Terms— Level sets; CT; Coronary Artery; Segmentation; Kissing Vessel Artifacts; Multiple regions competition

I. Introduction

Reliable and correct vessel segmentation is invaluable in the diagnosis of vascular disease, as it is a crucial and essential step for quantitative vessel analysis. Since their introduction as a means of front propagation based segmentation methods, active contour models have been extensively studied. Existing approaches can be categorised in two groups, in terms of the image driven energy, namely, edge based and region based models.

The application of edge based models to image segmentation was pioneered in [1], where active contours are represented using geodesic formulations. In these methods, the front evolution is terminated using image gradient information, and therefore, they are robust to region inhomogeneities but sensitive to image noise and contour initialisation. Statistical shape priors [2, 3], serving as external constraints in the active contour energy functional, are usually employed to improve the overall segmentation results of the edge based models, particularly in the case where intensity features are ambiguous. Contrary to edge-based models, which characterise image content based on a small neighbourhood of pixels, region-based methods, relying on global information obtained from image regions, are more robust to weak image gradients at the edge locations and image noise. The use of region based active contour models was firstly reported by Chan and Vese [4], who proposed an active contours model based on a simplified Mumford-Shah [5] functional. In their method, image regions are represented by their mean intensities. Hence, their method cannot distinguish objects with similar mean intensities but different variances. Exponential parametric models and non-parametric methods were later introduced to model complex intensity distributions [6, 7]. The aforementioned methods, however, are based on global intensity statistics, which are inefficient, when regional statistics are spatially varying across the image. Localised approaches [8-11], estimating regional statistics in a neighbourhood of the active contour, have recently emerged to address this problem. By introducing a localised kernel, such models are more robust to local intensity variations and can therefore improve the overall segmentation results under changing brightness conditions. However, segmentation based on local decisions alone may not suffice to drive the contour to terminate at the desired boundaries, since it may be trapped in undesired local stationary points. Moreover, the selection of appropriate scales for the localisation poses additional difficulties. We refer the reader to [12] and the references therein for the comprehensive review of the active contour based segmentation.

Another issue in the segmentation of vascular structures in angiography images is the so called “kissing vessel” artifacts [13], where vessels are in close proximity to each other. This is a partial volume effect, often encountered in angiograms [14], which may result in artificial vessel junctions, thus distorting the geometry of the vessel. Wong and Chung [15] proposed tracing the centrelines of vessels and segmenting their cross sections based on a probabilistic vessel axis tracing framework. Their approach accommodates the engagement of user’s interaction to produce desired traces through the abnormal regions, which contain kissing vessels, lesion vessels (e.g., stenosis) and vessel

This work was partially supported by a City University London Research Studentship.

Y. Wang is with the Information Engineering and Medical Imaging Group, City University, London, UK (e-mail: yin.wang.1@ city.ac.uk).

P. Liatsis is with the Information Engineering and Medical Imaging Group, City University, London, UK (phone: +44(0) 20 7040 8126; fax:+44 (0)20 7040 8568; e-mail: p.liatsis@city.ac.uk).

junctions. The final segmentation in such regions is thus derived from the continuous vessel axis based on the cross sections.

The contributions of the present work are two-fold. Firstly, we propose a new active contour based algorithm, which utilises both global and local intensity statistics to segment coronary arteries in CT angiographies. The application of local intensity information allows for accommodating uneven brightness distributions over the image. The global energy, designed as a normalised cumulative distribution function (CDF) based on the histogram of the input images, ensures that the contour evolves towards the desired boundaries without being trapped in local stationary points. Secondly, we develop a novel slice-by-slice correction scheme based on multiregion competition algorithms to suppress kissing vessel artifacts, which are not normally addressed in conventional segmentation approaches. To the best of our knowledge, the majority of the work published so far does not consider the effect of kissing vessel artifacts. However, such artifacts are inherent in coronary CT angiograms and should be addressed to produce morphologically correct vessel segmentations for other radiological tasks. Following this introduction, the proposed method is described in Section II. Next, experimental results on both synthetic and clinical datasets, demonstrating the efficiency and application of the proposed approach, are provided. Finally, the conclusions of this work and future research directions are presented in Section IV.

II. METHODS

In this section, we present an active contour based method for segmentation of the coronary arteries in 3D CTA images, where both global and local intensity information are utilised in the energy calculation. We compute the regional statistics locally, in the neighbourhood of the active contour, to deal with varying image brightness. The global intensity information, on the other hand, is utilised to evolve the contour to the desired boundaries without being trapped in local minima. The proposed algorithm is implemented using a Bayesian probabilistic framework to incorporate the two homogeneity constraints. Possible outliers, such as kissing vessel artifacts, are removed in the subsequent stage through a novel slice-by-slice correction scheme based on multiregion competition, where both arteries and kissing vessels are identified and tracked through the axial slices.

A. Modelling Regional Statistics

We commence our analysis by modelling the histogram of coronary CT images using a Gaussian Mixture Model (GMM) in a similar way as described by Yang and her co-workers [16], where three Gaussian functions were used to approximate the intensity distribution of the background (i.e., the air in the lungs), soft tissues and blood filled regions, respectively. The parameters for each class are determined by the Expectation Maximisation (EM) algorithm. By utilising prior anatomical knowledge that coronaries are located on the outer surface of the heart, we neglect the class corresponding to the air to obtain a bi-modal histogram (see Fig. 1(b)). The first peak (T_1) in the fitted histogram corresponds to the soft tissues in the heart. We therefore assume that voxels with intensity values less than T_1 belong to the background, while voxels with intensity values greater than this threshold are considered as potential objects of interest (i.e., blood-filled regions).

Based on the fitted histogram, we assign each voxel of the image with a fuzzy label, measuring the probability of the voxel belonging to the object, through the application of a labelling function. In this research, we formulate the labelling function as a normalised CDF of the histogram. We normalise the labelling function between -1 and 0 for voxels with intensity values between 0 to T_1, and bound the output of the function between 0 and 1 for the input voxels with intensity values greater than T_1. Let g(t) represent the PDF of the fitted histogram, as shown in Fig. 1(b). The label function is defined as a normalised CDF of the fitted histogram as:

$$L(x)=\begin{cases}\left(\int_{-\infty}^{x} g(t)dt \Big/ \int_{-\infty}^{T_1} g(t)dt\right)-1, & x\in(-\infty,T_1]\\ \int_{T_1}^{x} g(t)dt \Big/ \int_{T_1}^{+\infty} g(t)dt, & x\in(T_1,+\infty)\end{cases} \quad (1)$$

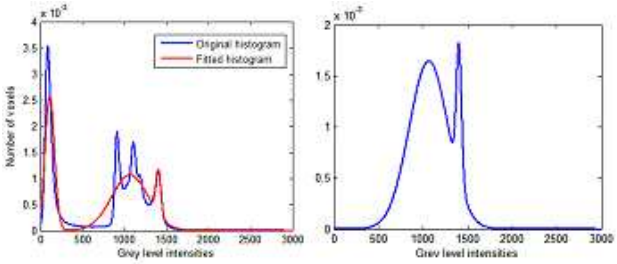

(a) (b)

Figure 1. The histogram of the CTA image. (a) The histogram (blue) and the fitted mixture model (red) of the CTA image. (b) The fitted histogram within the heart region.

Let $O_{\mathbf{x}}$ denote a neighbourhood with a radius r centred at **x**. The localised image, $O_{\mathbf{x}}$, can be partitioned into two sub-regions by the active contour, i.e., the regions inside and outside the active contour, respectively. Here, we define the probability of a voxel being classified to the region Ω_i as follows:

$$P_i = P(I(\mathbf{y}) \mid \mathbf{y}\in\Omega_i \cap O_{\mathbf{x}}) = \frac{1}{\sqrt{2\pi}\sigma_i}\exp\left(-\frac{(\mu_i - I(\mathbf{y}))^2}{2\sigma_i^2}\right) \quad (2)$$

where $\{\Omega_i \cap O_{\mathbf{x}} \mid i = 1,2\}$ denote the regions inside and outside the contour within the localised image $O_{\mathbf{x}}$, centred at **x** with a radius r. I(**y**) is the image intensity at **y**, μ_i and σ_i represent the mean and the variance derived from the region Ω_i, respectively.

As previous discussed, global statistics are robust to local spurious features, while local information is capable of dealing with spatially varying brightness in the image. In order to incorporate their advantages, the labelling function is designed to be a normalised CDF of the fitted histogram, rather than the probability density function (PDF) as defined in Yang et al. model [16]. By doing so, the distal segments of the arteries, usually exhibiting relatively lower intensities and less contrast to the background, would be assigned with labels which are

close to zero (i.e., $|L(\mathbf{x})| \rightarrow 0$). In these regions, the global energy term will contribute less to the overall energy functional, and thus, the contour will evolve mainly based on the local energy information. On the other hand, when the contour is located in homogenous regions or unwanted local minima, the global energy term is able to provide additional force to drive the front to evolve away from these stationary points.

B. Active Contour Energy and Level Set Formulation

In this section, we incorporate the two aforementioned energy terms using a probabilistic framework. Consider a contour $C(\mathbf{x})$ representing the boundary of the object to be segmented. For each point along the contour, given the local image $O_{\mathbf{x}}$ and the labelling function $L(\mathbf{y})$, the posterior probability of a voxel $\mathbf{x}$ being classified as belonging to the sub-region $\Omega_i \cap O_{\mathbf{x}}$ can be defined as:

$$P(\mathbf{y} \in \Omega_i \cap O_{\mathbf{x}} \mid I(\mathbf{y}), L(\mathbf{y})) = \frac{P(I(\mathbf{y}), L(\mathbf{y}) \mid \mathbf{y} \in \Omega_i \cap O_{\mathbf{x}}) P(\mathbf{y} \in \Omega_i \cap O_{\mathbf{x}})}{P(I(\mathbf{y}), L(\mathbf{y}))} \quad (3)$$

where $P(\mathbf{y} \in \Omega_i \cap O_{\mathbf{x}})$ is the prior probability of the current voxel being assigned to region Ω_i among all the possible partitions within the local image $O_{\mathbf{x}}$. This term can be ignored, if equal probabilities are assumed for all partitions of the image. $P(I(\mathbf{y}),L(\mathbf{y}))$ denotes the joint probability density distribution of the gray level value $I(\mathbf{y})$ and the labelling function $L(\mathbf{y})$, which are independent of the segmentation of the image and can therefore be neglected. We assume that the voxel labels and the regional gray level intensity distribution are independent. The posterior probability for each voxel can then be computed as:

$$P(I(\mathbf{y}), L(\mathbf{y}) \mid \mathbf{y} \in \Omega_i \cap O_{\mathbf{x}}) = P(I(\mathbf{y}) \mid \mathbf{y} \in \Omega_i \cap O_{\mathbf{x}}) P(L(\mathbf{y}) \mid \mathbf{y} \in \Omega_i \cap O_{\mathbf{x}}) \quad (4)$$

The prior probability of $P(I(\mathbf{y})|\mathbf{y} \in \Omega_i \cap O_{\mathbf{x}})$ has been defined in (2). In order to compute the posterior probabilities in (4), the prior probability of the labelling function should be known. In this research, we model the prior probability distribution of the labels as:

$$P(L(\mathbf{y}) \mid \mathbf{y} \in \Omega_i \cap O_{\mathbf{x}}) \propto \exp\left(\frac{v}{2} L(\mathbf{y}) R(\mathbf{x}) k_\sigma(\mathbf{x}, \mathbf{y})\right) \quad (5)$$

where

$$k_\sigma(\mathbf{x}, \mathbf{y}) = \frac{1}{\sqrt{2\pi}\sigma} \exp\left(-\frac{(\mathbf{x}-\mathbf{y})^2}{2\sigma^2}\right)$$

represents the weighting kernel, which is a decaying function of the distance between $\mathbf{x}$ and $\mathbf{y}$. v is the overall weight, which determines the influence of the labels on the segmentation, and $R(\mathbf{y})$ is a normalised Boolean function indicating whether the current voxel $\mathbf{y}$ is located inside the contour $C(\mathbf{x})$ within the local image $O_{\mathbf{x}}$:

$$R(\mathbf{x}) = \begin{cases} -1, \text{ if } \mathbf{x} \in \Omega_2 \cap O_{\mathbf{x}} \text{ (outside the contour)} \\ +1, \text{ if } \mathbf{x} \in \Omega_1 \cap O_{\mathbf{x}} \text{ (inside the contour)} \end{cases} \quad (6)$$

According to (5), when a voxel, located at position $\mathbf{x}$, is classified as belonging to the object, i.e., $R(\mathbf{x}) = 1$, then a point $\mathbf{y}$ in its vicinity has a high probability of being marked as belonging to the object (i.e., $L(\mathbf{y}) \rightarrow 1$) and is less likely to be considered as background ($L(\mathbf{y}) \rightarrow -1$).

Let ϕ denote the embedded level set function, and assume that the level set function takes positive values in the interior of the contour, and is negative for regions outside of the zero level set. To achieve the active contour segmentation, we need to define a contour $C(\mathbf{x})$ that minimises the energy along the contour over the image domain. We denote $H(\cdot)$ to be the Heaviside function, and then the active contour energy can be formulated as:

$$\begin{aligned} E = -\int H'(\phi(\mathbf{x})) \sum_{i=1}^{2} \{ \int_{\Omega_i \cap \Omega_{\mathbf{x}}} [\log P(I(\mathbf{y}) \mid \mathbf{y} \in \Omega_i \cap O_{\mathbf{x}}) \\ + \log P(L(\mathbf{y}) \mid \mathbf{y} \in \Omega_i \cap O_{\mathbf{x}}) d\mathbf{y}] M_i(\phi(\mathbf{y})) \} dx \\ + \mu \int |\nabla H(\phi(\mathbf{x}))| dx \end{aligned} \quad (7)$$

where $M_1(\phi(\mathbf{y}))=H(\phi)$ and $M_2(\phi(\mathbf{y}))=1-H(\phi)$, H' denotes the derivative of the Heaviside function. The first term on the right hand side of (7) is the negative logarithm posterior probability defined in (4), which would be minimised when the active contour is located on the desired boundaries. While the second term estimates the length of the zero level contour of the level set function, which enforces smoothness in the resulting contour. The constant μ controls the contribution of this smoothness term to the active contour functional. The associated Euler-Lagrange equation of (7) is defined as:

$$\frac{\partial \phi}{\partial t} = \delta(\phi(\mathbf{x})) \left(\mu \operatorname{div}\left(\frac{\nabla \phi(\mathbf{x})}{|\nabla \phi(\mathbf{x})|}\right) + \log \frac{P_1}{P_2} + v \int L(\mathbf{x}) k_\sigma(\mathbf{x}, \mathbf{y}) d\mathbf{y} \right) \quad (8)$$

where P_1 and P_2 were defined previously in (2). $\delta(\cdot)$ denotes the Dirac delta function, which is defined as the derivative of Heaviside function $H(\cdot)$.

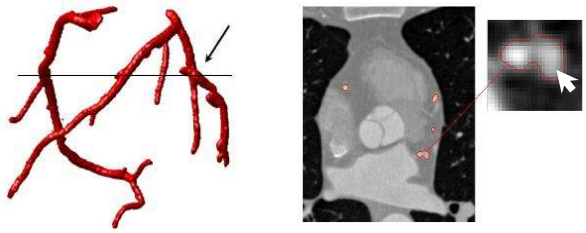

(a) (b)

Figure 2. Illustration of 'kissing vessel' artifacts present in coronary CT images. (a) 3D surface reconstruction of the coronary arteries with a touching non-arterial vessel (shown by the arrow), (b) The cross sectional image taken from the volume, and the close up image of the outlier vessel. The cross sectional segment of the non-arterial vessel appears (shown by the arrow) darker than the artery.

C. Slice-by-Slice Correction

The segmentation results obtained in the first stage of processing is nearly optimal. However, due to the complexity of medical images and the associated artifacts, the resulting images may contain some outliers, such as kissing non-arterial vessels (see Fig. 2). In order to remove these erroneous segments, a slice-by-slice correction scheme was applied to the resulting images obtained in the first stage of the segmentation. As it can be observed in the zoomed image in Fig. 2(b), the non-arterial

vessel appears darker than the coronary artery, and thus, it can be potentially segmented through a multiple regions based level set model. In region-based models, the active contour energy can be considered as the sum of two types of forces, namely, the shirking force and expanding force, respectively. The shrinking force, derived from image regions inside of the contour, is always negative. It tends to exclude the current point from the interior areas of the contour. The expanding force, on the other hand, is always positive, which tries to move the contour outwards in order to include the current point into the resulting segmentation. In this paper, we propose a modification to Brox and Weickert's evolution scheme [17], to let the active contour will evolve according to two-phase energy (competing with itself), when there is no competition nearby. When multiple contours are present in an interface, the points in the interface would move together, subject to the strongest force across all the regions. The proposed evolution equation is defined as follows:

$$\frac{\partial \phi_i}{\partial t} = \delta\phi_i \left\{ \max_{\substack{H'(\phi_j)>0 \\ i \neq j}} (e_{i,1}, e_{j,2}) - \max_{\substack{H'(\phi_j)>0 \\ i \neq j}} (e_{i,2}, e_{j,1}) \right\} \tag{9}$$

$$e_{k,1} = \log P_{k,1} + \frac{\mu}{2} \operatorname{div}\left(\frac{\nabla \phi_k}{|\nabla \phi_k|} \right)$$

$$e_{k,2} = \log P_{k,2} + \frac{\mu}{2} \operatorname{div}\left(\frac{\nabla \phi_k}{|\nabla \phi_k|} \right)$$

where $e_{k,1}$ and $e_{k,2}$ represent the active contour energy derived from regions within the interior and the exterior of the k-th level set function, respectively. $P_{k,i}$ denotes the posterior probability of a voxels, **x**, being classified as belonging to image regions $\Omega_i \bigcap O_{\mathbf{x}}$ by the k-th level set function, defined previously in (4).

To identify kissing vessels and remove them from the first stage of the segmentation, we assume that the coronary arteries can be modelled as a tree structure, and the transaxial cross sectional segments of the artery taken from the top to the bottom can only split but not merge over the transaxial images. The procedure begins by finding the first slice, which contains the coronary artery, as shown in Fig. 3(a). Next, we assign each connected object to a level set function in the starting slice and perform 2D active contour segmentation according to evolution equation in (8). To identify the presence of the kissing vessels, for each axial slice of the CT data, we compare the resulting 2D segmentation obtained from the previous slice against the initial segmentation defined in the first stage of the processing. If there is a component that does not touch any known segments of the tracked artery, then the object is considered as a kissing vessel structure. Fig. 3(b) shows the resulting 2D segmentation (red contours) obtained at the slice before the presence of the kissing vessels, while the initial segmentation at this slice is illustrated in Fig. 3(c). It can be seen that the kissing vessel (arrowed) in this slice is not connected to any known objects. Hence, this object is considered as the kissing vessels and a level set is assigned to it (shown in green contour in Fig.3 (d)). In the next step, both of these two vessels will be evolved based on (9) and tracked (see Fig. 3(e)). The process is repeated until the last slice containing the artery is reached.

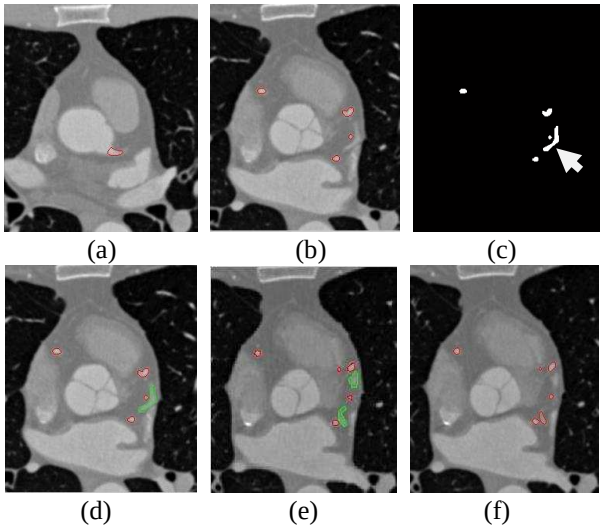

Figure 3. Transaxial slices illustrating the slice-by-slice correction algorithm. (a) The first slice containing the artery (delineated in red). (b) The artery is tracked through the slices. (c) The binary image obtained from the first stage segmentation; this is the first slice containing the kissing vessel (shown by the arrow), (d) and (e) The kissing vessel is identified and tracked over the slices (depicted by the green contours). (f) The same transaxial slice as shown in (e) depicting the initial segmentation.

III. Experimental Results and Discussion

In this section, we apply our method to both 2D synthetic and 3D and clinical images to analyse its efficiency. Firstly, we compare the proposed method with active contour models based on global and local information alone, to demonstrate the benefits offered by using both local and global statistics on a 2D synthetic image. Then, we validate the proposed method in 3D CTA images and compare it with Yang et al., method [16]. The tuning parameters of the proposed method were empirically determined and fixed throughout the experiments. In particular, we choose the smoothness weight μ to be equal 0.2, while the global energy factor v is set to 0.4. The radius of the localised image r is selected based on prior information regarding the size of the vessels to be segmented, which is equal to the maximum radius of the vessel of interest.

A. Experiments on Synthetic Images

Firstly, we use the synthetic image shown in Fig. 4(a) as an example to demonstrate the benefits offered by the proposed algorithm. The image consists of two elongated objects with distinct intensity distributions, which are close to each other. Gaussian noise was added to the images for a simplified approximation of the noise model in CT images.

The comparison of the efficiency in segmenting the object is conducted between the proposed algorithm, the localised CV model and Yang et al., method. Four metrics were used to validate the segmentation results, specifically:

$$TP = \frac{N_B \bigcap N_R}{N_R}, \quad FN = \frac{N_R - N_B \bigcap N_R}{N_R} \tag{10}$$

$$FP = \frac{N_B - N_B \bigcap N_R}{N_R}, OM = 2 \cdot \frac{N_B \bigcap N_R}{N_B + N_R}$$

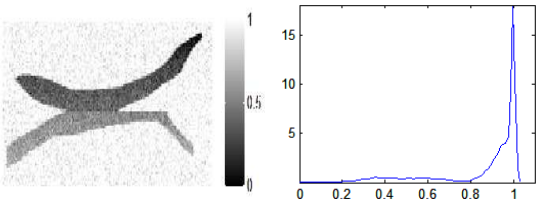

(a) (b)

Figure 4. A synthetic image to evaluate the efficiency of the proposed method. (a) Illustration of the synthetic image, (b) Histogram distribution.

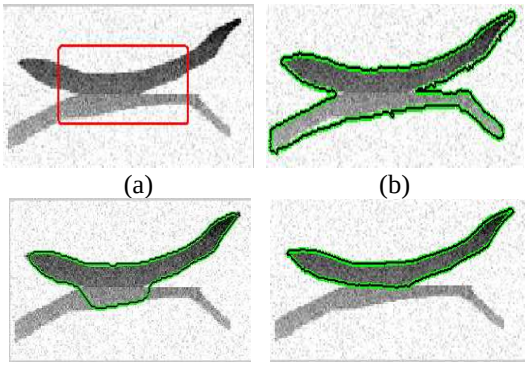

(a) (b)

(c) (d)

Figure 5. Comparison of the segmentation results obtained using various methods. (a) Initialisation, (b) Yang's model results, (c) Localised CV method results, (d) Results of the proposed algorithm.

TABLE I
COMPARISON OF THE 2D SYNTHETIC IMAGE SEGMENTATION RESULTS FOR VARIOUS METHODS

Rate	Yang et al. Method	Localised	Proposed Method
TP (%)	94.96	95.91	94.61
FN (%)	5.040	4.590	5.390
FP (%)	103.3	27.88	4.430
OM	0.6361	0.8571	0.9507

The ground truth data N_R is defined as a binary image with voxels labelled to one for the object and zero for others. N_B indicates the pixels/voxels, which are segmented as the object by the aforementioned algorithms. TP, FN and FP denote the true positive, false negative and false positive metrics, respectively. OM represents the overlapping metric defined in [18], which is close to 1, when the segmentation is well matched to the reference ground truth, and approaches to zero when the results have no similarity to the reference.

In Fig. 5, we present the segmentation results obtained using the previously reported algorithms and the proposed method for a 2D synthetic image. Contour initialisation is shown in Fig. 5(a). Fig. 5(b) shows that Yang et al. model, based on global intensity information alone, segments the two objects as a whole. The localised CV method achieves a better segmentation result. However, as shown in Fig. 5(c), there are regions which have been incorrectly segmented. The proposed method successfully extracts the desired object, as shown in Fig. 5(d). The quantitative validation of these results is shown in Table I. It can be seen that the TP rate of the proposed method is slightly lower than the other two models. This is due to the fact that both of these methods over-segment the object, where more pixels are classified as belonging to the object, thus resulting in a higher TP rate. However, in terms of the FP and OM metrics, the performance of the proposed method is superior.

B. Experiments on Real Clinical Images

Eight coronary CT volumes were acquired from St Thomas and Guys Hospitals, London, UK. Two of them were obtained with a 16-slice CT scanner (Brilliance, Philips), and the remaining six volumes were acquired with a Philips ICT-256 workstation. In addition, another four coronary CT studies were obtained from a public database [19]. The mean size of the images is 512 ×512 × 286 with an average in-plane resolution of 0.40 mm × 0.40 mm, and the mean voxel size in the z-axis is 0.42 mm. The ground truth data were obtained through manual delineation. Since the manual segmentation procedure is very time consuming, only four major branches, i.e., right coronary artery (RCA), left anterior descending artery (LAD), left circumflex artery (LCX), and one large side branch of the coronaries, were chosen for evaluation. In addition to the metrics defined in (10), the Hausdorff distance [20] was applied to measure the difference between the segmented vessel surface and the manually delineated ground truth data. The Hausdorff distance is defined as:

$$d_H(\mathbf{X},\mathbf{Y}) = \max\{\sup_{x\in\mathbf{X}}\inf_{y\in\mathbf{Y}} d(x,y), \sup_{y\in Y}\inf_{x\in\mathbf{X}} d(x,y)\} \qquad (11)$$

where **X**,**Y** are the vertices of the mesh surfaces of the arteries corresponding to the segmentation results and the ground truth, respectively, and d(x,y) measures the Euclidean distance between points x and y belonging to vertices **X** and **Y**. The mesh surface of the arteries was obtained by extracting the isosurface of the binary volume obtained from the segmentation/manual delineation, using the marching cube algorithm [21] .

In Fig. 6 and Tables II and III, we present the comparison of the resulting segmentation results obtained using the proposed method and Yang's method with respect to the ground truth data. The initial surface for the level set evaluation was obtained using a Hessian-based vessel enhancement filter. The tuning parameters of both of the two techniques were empirically determined from a training set, which consisted of three CT studies randomly selected from the available datasets. The proposed approach was implemented in MATLAB (R2010b) on a standard specification PC (Dell Precision T3500, Inter(R) Xeon(R) CPU at 2.67GHz), and the average execution time was found to be 80 seconds for extraction of the entire coronary trees. Yang et al., on the other hand, requires roughly 45 seconds to carry out the same process.

As shown in Table II, the mean TP rate and OM metric for the proposed method were found to be 91.1% and 0.776, respectively, which indicate that the proposed method is able to correctly extract the major branches of the coronary arteries. Meanwhile, high values of the FP rate (39.2% on average) mean that the proposed method over-segments the arteries (see Figs. 6(a) and (c)). This is because the ground truth data were modelled as circular cross sectional tubes, which leads to the resulting ground truth data under-estimating the true vessel

surface. However, in terms of the voxel-wise measurement, the average value of the Hausdorff distance metric was found to be 0.73 voxels, which implies that the proposed method is capable of extracting the luminal surfaces of the arteries with sub-voxel accuracy.

TABLE II
COMPARISON OF THE 3D CTA SEGMENTATION RESULTS BETWEEN THE PROPOSED METHOD AND YANG'S TECHNIQUE

Rate	Methods	
	Proposed Method Mean	Yang et al. Method Mean
TP (%)	91.1	53.8
FP (%)	39.3	16.9
OM	0.776	0.556
Mean(d_H)	0.730	1.07

TABLE III -A
COMPARISON OF THE 3D CTA SEGMENTATION RESULTS BETWEEN THE PROPOSED METHOD AND YANG'S TECHNIQUE: DATASETS #1-6

Rate	Methods	3D CTA Images					
		1	2	3	4	5	6
TP (%)	Proposed	**94.1**	**93.9**	**93.1**	**92.8**	**97.0**	**93.2**
	Yang's	47.6	50.3	52.1	25.6	89.9	87.9
FP (%)	Proposed	**32.4**	**28.4**	**43.1**	**38.3**	**45.5**	**29.4**
	Yang's	1.31	8.39	13.6	3.16	60.7	68.9
OM	Proposed	**0.831**	**0.731**	**0.791**	**0.803**	**0.800**	**0.837**
	Yang's	0.639	0.634	0.629	0.397	0.717	0.685
Mean(d_H)	Proposed	**0.623**	**1.02**	**0.670**	**0.833**	**0.623**	**0.782**
	Yang's	0.865	1.35	1.00	1.09	0.767	0.891

TABLE III -B
COMPARISON OF THE 3D CTA SEGMENTATION RESULTS BETWEEN THE PROPOSED METHOD AND YANG'S TECHNIQUE: DATASETS #7-12

Rate	Methods	3D CTA Images					
		7	8	9	10	11	12
TP (%)	Proposed	**90.1**	**89.0**	**95.3**	**80.5**	**86.5**	**87.8**
	Yang's	51.2	49.2	88.4	53.6	23.4	26.7
FP (%)	Proposed	**41.6**	**38.6**	**51.8**	**35.2**	**42.2**	**44.7**
	Yang's	3.16	1.57	16.3	10.0	9.55	6.18
OM	Proposed	**0.778**	**0.782**	**0.713**	**0.744**	**0.756**	**0.755**
	Yang's	0.663	0.318	0.580	0.655	0.353	0.402
Mean(d_H)	Proposed	**0.759**	**0.719**	**0.620**	**0.561**	**0.769**	**0.783**
	Yang's	1.07	1.63	0.976	1.15	1.24	0.861

In terms of the FP rate, Yang et al. method performs better than the proposed approach, with the average value found to be 16.9%. However, we note that the TP and OM metrics of their segmentation are significantly lower than the proposed one, with the average values being 53.8% and 0.556, respectively. In addition, by observing the statistics presented in Table III, we note that both the TP rate and the OM metric vary significantly, with the TP rate ranging from 23.4% to 89.9%, while the minimum and maximum values of the OM metric were found to be 0.318 and 0.717, respectively. These observations imply that Yang et al. algorithm under-segments the coronary arteries and is only able to extract partial branches of the arterial tree, which are illustrated in Figs. 6(b) and (d). The reason for this is that Yang et al. method, solely relying on global intensity statistics, is sensitive to image contrast and brightness changes. Their model can correctly extract the arteries when the intensity densities are evenly distributed along the vessel. However, uneven intensity distribution is commonly encountered in coronary CTA, because of the concentration attenuation of the contrast agent and acquisition noise. In this case, Yang et al. method can only extract the proximal segments of the arteries, since distal segments have relatively lower intensity values and lack image contrast.

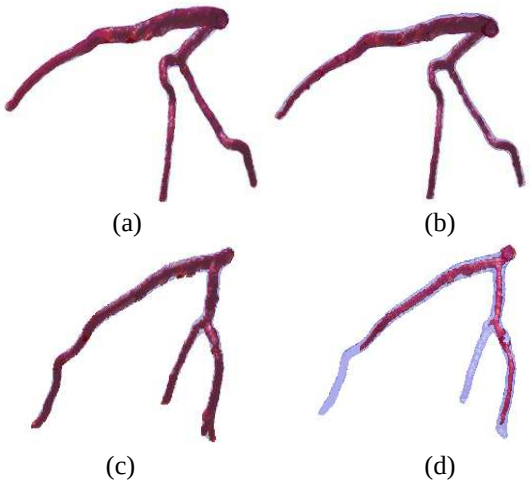

Figure 6. Comparison of the resulting segmentation for datasets #5 and #11 obtained using the proposed model (a) and (c), and Yang's method (b) and (d), with respect to the ground truth data. The blue surface represents the manually delineated ground truth data, while the resulting segmentations are shown in red.

TABLE IV
COMPARISON OF THE SEGMENTATION RESULTS BEFORE AND AFTER THE APPLICATION OF THE CORRECTION SCHEME DATA #7

Rate	Before correction	After correction
TP (%)	82.4	85.3
FN (%)	17.6	14.7
FP (%)	294	22.9
OM	0.380	0.820

Two CTA studies were affected by the presence of kissing vessels (i.e., datasets #7 and #11). The slice-by-slice correction scheme was subsequently applied after the first stage of the segmentation. Since the kissing vessels only affect the coronary arterial tree locally, we only conduct our analysis on the vessel segments containing kissing vessels. As illustrated in Fig. 7, the kissing vessel artifact was identified next to the distal LCA branch, between cross section A and C. To evaluate the performance of the proposed algorithm, we firstly slice the vessel segment by a sequence of 2D planes, which are normal to the course of the vessel, as shown in Fig. 7(a). Then, we compare the resulting segmentations obtained with and without the slice-by-slice correction against manually delineated boundaries on these cross sectional images. As depicted in Fig. 7(b), the bounds of the artery before and after the application of the correction are depicted in black and blue, respectively, and the manual segmentation is shown in red. Fig. 8 illustrates the 3D surface reconstruction image before and after applying the slice-by-slice correction algorithm, it can be seen that the false positives, i.e., the kissing vessels (arrowed), is removed from the first stage of the segmentation. Four metrics, as defined in (10), were used to quantify the performance of the algorithm, and the results are shown in Table IV. It can be seen that the FP rate, which is primarily caused by the kissing vessels, is

dramatically reduced (from 294% to 22.9% for these segments containing kissing vessels, e.g., the vessel segments shown in Fig. 7, between cross sections A and C), through the use of the slice-by-slice correction algorithm.

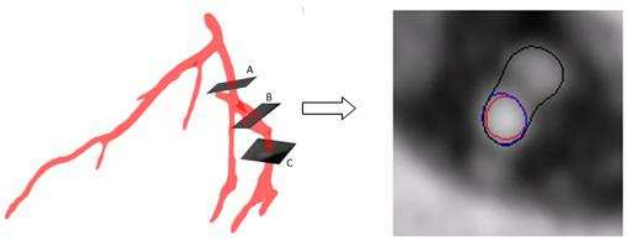

(a) (b)

Figure 7. The efficiency of the proposed slice-by-slice correction algorithm demonstrated by cross sectional view image. (a) 3D volume data, and (b) Cross sectional view image randomly taken from the 3D volume data (cross section B), illustrating the resulting segmentations with and without the correction step are shown in blue and black, respectively. The red contour represents the reference boundaries of the vessel obtained through manual delineation.

(a) (b)

Figure 8. The comparison (a) before and (b) after the correction process (datasets #7). The touching non-arterial vessel (arrowed) has been removed.

IV. CONCLUSIONS AND FUTURE WORK

Accurate extraction of coronary arteries is important for assessment of arterial lesions in clinical practice. In this paper, a novel two-step algorithm was proposed to efficiently segment coronary arteries from CT images by making use of both global and local intensity statistics. The global energy was designed as a normalised CDF based on the histogram of the input image data, which adapts its contribution to the overall active contour energy by considering the spatial-varying properties of the artery. The kissing vessels are identified and tracked throughout axial slices in the second stage of the segmentation based on a multiregion competition algorithm. Experiment on synthetic image has shown that our method is capable of segmenting the object of interest without being trapped by local stationary features. For the clinical data, the results show that the proposed approach is able to correctly segment the major branches of the arterial tree, with an average distance to the manually delineated ground truth of 0.73 voxels. Furthermore, in the presence of kissing vessel artifacts, the performance of the segmentation is significantly improved by the slice-by-slice correction scheme.

In terms of future research, we intend to conduct quantitative coronary analysis based on the segmented images and construct patient-specific arterial models, which would further assist the clinician in diagnosis of coronary disease.

ACKNOWLEDGMENT

The authors would like to acknowledge Dr Gerry Carr-White and Rebecca Preston at St Thomas and Guys Hospitals London for their invaluable advice and the provision of the CTA datasets.

REFERENCES

[1] V. Caselles, et al., "Geodesic Active Contours," International Journal of Computer Vision, vol. 22, pp. 61-79, 1997.

[2] M. E. Leventon, et al., "Statistical Shape Influence in Geodesic Active Contours," in Proc. of 5th IEEE EMBS International Summer School on Biomedical Imaging, USA, 2002, pp. 8-18.

[3] Y. Chen, et al., "Using Shape Priors in Geometric Active Contours in a Variational Framework," International Journal of Computer Vision, vol. 50, pp. 315-328, 2002.

[4] T. F. Chan and L. A. Vese, "Active Contours Without Edges," IEEE Transacation on Image Processing, vol. 10, pp. 266-277, 2001.

[5] D. Mumford and J. Shah, "Optimal Approximations by Piecewise Smooth Functions and Associated Variational Problems," in Proc. of Communications on Pure and Applied Mathematics, 1989, pp. 577-685.

[6] F. Lecellier, et al., "Region based Active Contours with Exponential Family Observations," Journal of Mathematical Imaging and Vision, pp. 28-45, 2010.

[7] J. Kim, et al., "A Non-parametric Statistical Methods from Image Segmentation using Information Theory and Curve Evolution," IEEE Transacation on Image Processing, vol. 14, pp. 1486-1502, 2005.

[8] M. W. K. Law and A. C. S. Chung, "Weighted Local Variance-Based Edge Detection and Its Application to Vascular Segmentation in Magnetic Resonance Angiography," IEEE Transacation on Medical Imaging, vol. 26, pp. 1224-1241, 2007.

[9] C. Li, et al., "Implicit Active Contours Driven by Local Binary Fitting Energy," in Proc. of IEEE Conference on Computer Vision and Pattern Recognition, 2007, pp. 1-7.

[10] C. Li, et al., "Minimization of Region Scalable Fitting Energy for Image Segmentation," IEEE Transacation on Image Processing, vol. 17, pp. 1940-1949, 2008.

[11] S. Lankton and A. Tannenbaum, "Localizing Region-Based Active Contours," IEEE Transacation on Image Processing, vol. 17, pp. 2029-2039, 2008.

[12] N. P. Tiilikainen, "A Comparative Study of Active Contour Snakes," 2007.

[13] O. Wink, et al., "Fast delineation and visualization of vessels in 3D angiographic images," IEEE Transacation on Medical Imaging, vol. 19, pp. 337-346, 2000.

[14] B. F. Tomandl, et al., "The “kissing vessel”-artifact: a problem occurring in the visualization of intracranial aneurysms using volume rendering and virtual endoscopy," Journal of Radiology, vol. 213, pp. 311-314, 1999.

[15] W. C. K. Wong and A. C. S. Chung, "Probabilistic Vessel Axis Tracing and its Application on Vessel Segmentation with Stream Surface and Minimum Cost Paths," Medical Image Analysis, vol. 11, pp. 567-587, 2007.

[16] Y. Yang, et al., "Automatic Segmentation of Coronary Arteries using Bayesian Driven Implicit Surfaces," in Proc. of 4th IEEE International Symposium on Biomedical Imaging, 2007, pp. 189-192.

[17] T. Brox and J. Weickert, "Level Set Segmentation with Multiple Regions," IEEE Transacation on Image Processing, vol. 15, pp. 3213-3218, 2006.

[18] A. Zijdenbos, et al., "Morphometric Analysis of White Matter Lesions in MR Images: Methods and Validation," IEEE Transacation on Medical Imaging, vol. 13, pp. 716-724, 1994.

[19] OsiriX. DICOM sample image sets [Online]. Available: http://pubimage.hcuge.ch:8080/

[20] R. T. Rockafellar and R. J.-B. Wets, Variational Analysis vol. 317. New York, NY, USA: Springer Press, 1998.

[21] W. Lorensen and H. E. Cline, "Marching Cubes: A High Resolution 3D Surface Construction Algorithm," Computer Graphics, vol. 21, pp. 163-170, 1987.